Collocated Finite Volume Scheme for Scalable Simulation of Induced Seismicity

Novikov, A.; Voskov, D.V.; Hajibeygi, H.; Jansen, J.D.

DOI
10.3997/2214-4609.202244103

Publication date
2022

Document Version
Final published version

Published in
European Conference on the Mathematics of Geological Reservoirs 2022

ECMOR 2022
European Conference on the Mathematics of Geological Reservoirs
EAGE

Collocated Finite Volume Scheme for Scalable Simulation of Induced Seismicity

A. Novikov[1], D. Voskov[1], H. Hajibeygi[1], J.D. Jansen[1]

[1] Delft University of Technology

Summary

An increasing number of geo-energy applications require the quantitative prediction of hydromechanical response in subsurface. Integration of mass, momentum, and energy conservation laws becomes essential for performance and risk analysis of enhanced geothermal systems, stability assessment of CO2 sequestration and hydrogen storage, resolving the issue of induced seismicity. The latter problem is of particular interest because it exposes safety risks to people and surface infrastructure.

Implicit coupling of conservation laws is computationally demanding and the solution procedure often uses different numerical methods for different laws that complicates simulation. Recently developed Finite Volume (FV) schemes for poromechanics present a unified approach for the modeling of conservation laws in geo-energy applications. Contact mechanics at faults requires special attention due to the inequality constraints it imposes and nonlinear friction laws that strongly affect the occurrence of seismicity.

We develop a cell-centered FV scheme for the purpose of integrated simulation in Delft Advanced Research Terra Simulator (DARTS) platform. The scheme proposes a unified numerical framework capable to resolve conservation laws in a fully implicit manner using a single collocated grid. Coupled multi-point flux and multi-point stress approximations provide mass, momentum, and heat fluxes at the faces of the computational grid. We use a conformal discrete fracture model to incorporate faults, where the multi-point approximations of fluxes respect the discontinuity in displacements. The block-partitioned preconditioner that takes the advantage of linear structure of the coupled problem is developed to facilitate the performance of the simulation.

The proposed numerical scheme are validated against analytical and numerical solutions in a number of test cases. The convergence and stability of the schemes are investigated. It is found that the developed scheme is indeed accurate, stable, and efficient. Thereafter, we demonstrate the applicability of the approach to model fault reactivation at the laboratory scale. In a core injection test, we validate the results of simulation against experimental measurements. Next, we investigate the performance of the different preconditioning strategies. The proposed block-partitioned preconditioning strategy demonstrates the scalability and efficiency of the numerical framework.

Introduction

Geomechanics plays an important role in safe and optimal subsurface operations related to geo-energy applications (Zoback, 2007). Changes in subsurface conditions (e.g., pressure depletion during gas production) often lead to subsidence and may initiate induced seismicity and serious damage to surface infrastructures (Segall et al., 1994; Shapiro et al., 2011; Jha and Juanes, 2014; Guglielmi et al., 2015; Buijze et al., 2020a). In geothermal operations, the re-injection of cooler fluid causes stress and strain changes that can potentially activate faults and lead to induced seismic activity (Buijze et al., 2020b). Successful and risk-controlled exploitation of subsurface resources, therefore, depends highly on the development of robust and efficient computational techniques for modeling geomechanics to design safe bounds of operation.

Recently, the Finite Volume Method (FVM) has gained considerable attention as a technique for modeling geomechanics, especially when mechanical interactions are modeled in a fully coupled manner with transport processes. The FVM is an attractive choice because it represents an integral form of conservation laws. Recent literature includes the development of the FVM for geomechanical simulations with both staggered (Deb and Jenny, 2017a; Sokolova et al., 2019; Shokrollahzadeh Behbahani et al., 2022) and collocated grids (Nordbotten, 2014; Berge et al., 2020; Terekhov and Tchelepi, 2020).

The coupled modeling of mechanics and flow in fractured media is another focus of intensive research. The Conformal Discrete Fracture Model (DFM) (Karimi-Fard et al., 2004) allows lower-dimensional faults to be resolved explicitly at the interfaces of equidimensional control volumes. It respects fault geometry and material contrasts in the vicinity of the fault. In contrast to DFM, the Embedded Discrete Fracture Model (EDFM) (Li and Lee, 2008) and projection-based EDFM (Tene et al., 2017) do not require conformal meshing of faults, hence, independent grids for faults and rock matrix can be employed. A comprehensive review and benchmarking study has been presented in Berre et al. (2021).

Both concepts have been successfully applied to mechanics and poromechanics modeling (Garipov and Hui, 2019; Terekhov and Vassilevski, 2022; Deb and Jenny, 2017b; Xu et al., 2021). In the embedded models, special discontinuity basis functions are used to resolve contact mechanics (Deb and Jenny, 2017b; Xu et al., 2021) whereas the use of vertex-based (Garipov et al., 2016; Garipov and Hui, 2019) grids allows for natural treatment of the discontinuities within a DFM unstructured mesh. In this paper, we employ the combination of an equidimensional DFM for the flow equation and a lower-dimensional representation of faults in mechanics as a contact problem. Contact mechanics imposes inequality constraints at faults. A penalty method with a return-mapping algorithm (Simo and Laursen, 1992; Garipov et al., 2016; Gallyamov et al., 2018), Lagrange multipliers (Simo and Laursen, 1992; Berge et al., 2020) or Nitsche method (Garipov and Hui, 2019) can be used to satisfy these constraints.

Induced seismicity occurs at critically stressed natural faults in the subsurface prone to unstable slip. This behavior of faults can be explained with nonlinear friction laws (Dieterich, 1979; Ruina, 1983; Chen and Spiers, 2016). Incorporation of these friction laws along with contact inequality constraints in the numerical model as boundary conditions is challenging. Instead, the introduction of additional unknowns at faults, e.g. displacements (Ucar et al., 2018), Lagrange multipliers (Berge et al., 2020) or gap vector (Novikov et al., 2022), provides more flexibility and seems natural once coupled with flow. Moreover, having the gap vector as a primary unknown eases the practical realization of friction laws since it does not require extra stabilization due to the presence of dual variables, i.e. Lagrange multipliers.

In this study, we develop a collocated fully implicit multi-point FVM scheme for poromechanics simulation of faulted porous media subject to nonlinear friction laws. We improve the formulation of multi-point approximations in faulted porous media presented in Novikov et al. (2022). In contrast to previous work, we impose continuity conditions for flow and mechanics at different points that are aligned with their fault representations. The resulting scheme can be used to solve arbitrarily anisotropic poromechanics problems on unstructured polyhedral grids in the presence of material heterogeneity. We use a penalty method with a return-mapping algorithm to resolve the contact problem. In order to validate the

numerical solution we consider a pair of benchmarks where we perform comparisons against analytics for a displaced reservoir setup (Jansen and Meulenbroek, 2022) and against laboratory measurements in a core injection experiment (Wang et al., 2020a). In the latter case, we first match experimental data with friction coefficients taken from the experiment and thereafter we reproduce the frictional response with a rate-dependent friction law.

The developed methods are implemented in the Delft Advanced Research Terra Simulator (DARTS). DARTS is a scalable parallel simulation framework, which has been successfully applied for modeling of hydrocarbon (Khait and Voskov, 2018a; Lyu et al., 2021a), geothermal (Khait and Voskov, 2018b; Wang et al., 2020b) and CO_2 sequestration (Kala and Voskov, 2020; Lyu et al., 2021b) applications. This study adds geomechanical capabilities to the existing advanced simulation capacity of DARTS, making it a fully thermo-hydro-chemical-mechanical (THCM) simulator for complex energy transition applications.

Continuous governing equations

Momentum and mass balance laws govern the coupling between mechanics and fluid flow in porous media. In the case of single-phase flow, the coupled system of equations (Coussy, 2003) reads

$$-\nabla \cdot \boldsymbol{\Sigma} = \rho_t g \nabla z, \tag{1}$$

$$\frac{\partial}{\partial t}(\phi \rho_f) + \nabla \cdot (\rho_f \boldsymbol{v}) + r = 0, \tag{2}$$

The system is subject to the relations defined in Coussy (2003); Zhao and Borja (2020), that represent

- the stress changes within an anisotropic poroelastic medium

$$\boldsymbol{\Sigma} - \boldsymbol{\Sigma}_0 = \mathbb{C} : (\boldsymbol{E} - \boldsymbol{E}_0) - (p - p_0)\boldsymbol{B}, \tag{3}$$

- the porosity associated with anisotropic poroelasticity

$$\phi - \phi_0 = \frac{\psi - \phi_0}{K_r}(p - p_0) + \boldsymbol{B} : (\boldsymbol{E} - \boldsymbol{E}_0), \tag{4}$$

- the infinitesimal strains

$$\boldsymbol{E} = \frac{\nabla \boldsymbol{u} + (\nabla \boldsymbol{u})^T}{2}, \tag{5}$$

- the Darcy velocity

$$\boldsymbol{v} = -\frac{\boldsymbol{K}}{\mu_f}(\nabla p - \rho_f g \nabla z), \tag{6}$$

- the properties of the matrix and fluid

$$\rho_t = \phi \rho_f + (1 - \phi)\rho_s, \quad \rho_f = \rho_f(p), \quad \mu_f = \mu_f(p). \tag{7}$$

In the above equations the subscripts f and s refer to the fluid and skeleton (porous rock), respectively, while $\nabla\cdot$ is the divergence operator and ∇ is the gradient operator. The rest of the notation is described in the Nomenclature section.

The subscript "0" denotes the reference state of a variable, i.e.,

$$\boldsymbol{\Sigma}_0 = \boldsymbol{\Sigma}(\boldsymbol{u}_0, p_0), \quad \phi_0 = \phi(\boldsymbol{u}_0, p_0), \quad \boldsymbol{E}_0 = \boldsymbol{E}(\boldsymbol{u}_0, p_0). \tag{8}$$

For the stress tensor the following relation holds

$$\boldsymbol{\Sigma} = \boldsymbol{\Sigma}' - p\boldsymbol{I} = \boldsymbol{\Sigma}'' - p\boldsymbol{B}, \tag{9}$$

where $\boldsymbol{\Sigma}'$ is the Terzaghi effective stress tensor and $\boldsymbol{\Sigma}''$ is the Biot effective stress tensor.

We note that the full Biot tensor results from general thermodynamic assumptions to a poroelastic medium, but in most practical applications it is only possible to experimentally determine a single scalar Biot coefficient. However, we maintain the full Biot tensor formulation because of its potential relevance to upscaling.

We denote vectors with bold lowercase letters, second-order tensors and matrices with bold capital letters, and the tensors of rank higher than two with script font. We also use the following definition for the total traction vector $\boldsymbol{f}$ and fluid flux q_f over an interface δ with unit normal $\boldsymbol{n}$:

$$\boldsymbol{f}|_\delta = -\boldsymbol{\Sigma}|_\delta \cdot \boldsymbol{n}_\delta = -\left(\mathbb{C} : \frac{\nabla \boldsymbol{u} + (\nabla \boldsymbol{u})^T}{2} - p\boldsymbol{B}\right)\Big|_\delta \cdot \boldsymbol{n}, \tag{10}$$

$$q_f|_\delta = -\boldsymbol{K}\left(\nabla p - \rho_f g \nabla z\right)\big|_\delta \cdot \boldsymbol{n}. \tag{11}$$

Boundary conditions for the system of Eqs. (1), (2) can be written as

$$\boldsymbol{n}^T\left(\alpha_n \boldsymbol{u}_\delta + \beta_n \boldsymbol{f}_\delta\right) = \gamma_n, \tag{12}$$

$$\left(\boldsymbol{I} - \boldsymbol{n}\boldsymbol{n}^T\right)\left(\alpha_t \boldsymbol{u}_\delta + \beta_t \boldsymbol{f}_\delta\right) = \boldsymbol{\gamma}_t, \tag{13}$$

$$\alpha_p p_\delta + \beta_p \left(\frac{q_f}{\mu_f}\right)_\delta = \gamma_p, \tag{14}$$

where subscript δ denotes the property evaluated at the boundary, α_n, β_n, α_t, β_t, α_p and β_p are coefficients that determine the magnitude of corresponding boundary conditions, while $\gamma_n, \boldsymbol{\gamma}_t, \gamma_p$ are the corresponding condition values. Eqs. (12), (13) represent normal and tangential boundary conditions for the momentum balance respectively, while Eq. (14) defines the boundary condition for mass balance. Eqs. (12)-(14) can describe a broad range of possible boundary conditions including Dirichlet ($\alpha_n = \alpha_t = 1, \beta_n = \beta_t = 0$), distributed force loading ($\alpha_n = \alpha_t = 0, \beta_n = \beta_t = 1$), free boundary ($\alpha_n = \alpha_t = \gamma_n = 0, \beta_n = \beta_t = 1, \boldsymbol{\gamma}_t = \boldsymbol{0}$), and roller conditions ($\alpha_n = \beta_t = 1, \beta_n = \gamma_n = \alpha_t = 0, \boldsymbol{\gamma}_t = \boldsymbol{0}$) for mechanics; and Dirichlet ($\alpha_p = 1, \beta_p = 0$) and Neumann ($\alpha_p = 0, \beta_p = 1$) conditions for flow.

At the fault interfaces we consider a gap vector $\boldsymbol{g}$ that is equal to the jump of displacements over the contact $\boldsymbol{g} = \boldsymbol{u}^+ - \boldsymbol{u}^-$, where $+/-$ denote a particular side of the fault. The contact conditions following Simo and Laursen (1992) read

$$g_N \leq 0, \tag{15}$$

$$\boldsymbol{f}'_T - \mu f'_N \frac{\dot{\boldsymbol{g}}_T}{|\dot{\boldsymbol{g}}_T|} = \boldsymbol{0}, \quad \Phi = 0, \quad |\dot{\boldsymbol{g}}_T| \neq 0, \quad \text{(slip)}, \tag{16}$$

$$\dot{\boldsymbol{g}}_T = \boldsymbol{0}, \quad \Phi < 0, \quad \text{(stick)}, \tag{17}$$

where $f'_N = \boldsymbol{n}^T \boldsymbol{f}'$ and $\boldsymbol{f}'_T = (\boldsymbol{I} - \boldsymbol{n}\boldsymbol{n}^T)\boldsymbol{f}'$ are the scalar normal and vectorial tangential projections of $\boldsymbol{f}'$ on the fault; g_N and $\boldsymbol{g}_T$ are the equivalent normal and tangential projections of $\boldsymbol{g}$ on the fault; $\dot{\boldsymbol{g}}$ stands for the time derivative of the gap vector and $\Phi = |\boldsymbol{f}'_T| - \mu f'_N$ is the Coulomb friction function with μ the friction coefficient. Eq. (15) represents a non-penetration condition, Eq. (16) governs relaxation of tangential traction once slip occurs, and Eq. (17) sets the change of the tangential gap (i.e. the slip) to zero if the slip criterion is not exceeded.

We consider two models of contact friction represented by friction laws as

$$\mu = \mu_s, \quad \text{(static)}, \tag{18}$$

$$\mu = \mu^* + (a - b)\ln\left(\frac{\dot{\boldsymbol{g}}_T}{v^*}\right) \quad \text{(steady-state)}, \tag{19}$$

where μ_s is the static friction factor, D_c is the critical slip distance, μ^* is a reference friction coefficient measured at reference velocity v^*, while *aandb* are the parameters of the rate-and-state friction law (Dieterich, 1979; Ruina, 1983).

Discrete equations

We use the Finite Volume Method (FVM) to discretize the balance equations. The Finite Volume (FV) scheme for Eqs. (1), (2) in cell i can be written in the following vector form

$$V_i \mathfrak{a}_i + \sum_{j \in \partial V_i} \delta_{ij} \mathfrak{f}_{ij} = \mathbf{0}, \tag{20}$$

where subscript j denotes the neighbours of the cell i, Δt is the time step size, V_i is the volume of cell i, δ_{ij} denotes the area of the connection between cells i and j. The accumulation vector $\mathfrak{a}_i$ and the vector of fluxes $\mathfrak{f}_{ij}$ in cell i are defined as

$$\mathfrak{a}_i = \begin{pmatrix} \Delta t \rho_{t,i}^{n+1} g \nabla z \\ (\tilde{\phi}\rho_f)\big|_{i,n}^{i,n+1} + \Delta t r_i^{n+1} \end{pmatrix}, \quad \mathfrak{f}_{ij} = \begin{pmatrix} \Delta t \boldsymbol{f}_{ij}^{n+1} \\ \rho_{fi} \tilde{q}_{f_{ij}}\big|_n^{n+1} + \Delta t (\rho_f q_f / \mu_f)_{ij}^{n+1} \end{pmatrix}, \tag{21}$$

where superscripts n, and $n+1$ denote the variables taken from the current and next time step, respectively, $\boldsymbol{f}$ is defined in Eq. (10), $\tilde{\phi}$ and $\tilde{q}_{f_{ij}}$, are defined as

$$\tilde{\phi} = \phi_0 + \frac{\psi - \phi_0}{K_r}(p - p_0), \quad \tilde{q}_{f_{ij}} = \Big((\boldsymbol{u} - \boldsymbol{u}_0)_{ij} - (\boldsymbol{u} - \boldsymbol{u}_0)_i \Big) \cdot (\boldsymbol{B}\boldsymbol{n})_{ij}, \tag{22}$$

where the following relations are used

$$\boldsymbol{B} : (\boldsymbol{E} - \boldsymbol{E}_0) = \boldsymbol{B} : \nabla(\boldsymbol{u} - \boldsymbol{u}_0) = \nabla \cdot \boldsymbol{B}(\boldsymbol{u} - \boldsymbol{u}_0) - (\boldsymbol{u} - \boldsymbol{u}_0) \cdot \nabla \cdot \boldsymbol{B}. \tag{23}$$

Here $\boldsymbol{B}$ is assumed to be symmetric, the porosity in Eq. (4) is treated as $\phi = \tilde{\phi} + \boldsymbol{B} : \nabla(\boldsymbol{u} - \boldsymbol{u}_0)$ and the last term is approximated using Gauss' formula as a sum of fluxes $\tilde{q}_{f_{ij}}$ over cell interfaces. The term $(\rho_f / \mu_f)_{ij}$ is calculated using an upwind approximation while the approximations of $\boldsymbol{f}_{ij}, q_{f_{ij}}$ and $\tilde{q}_{f_{ij}}$ are discussed in the next sections.

To satisfy Eqs. (15)-(17), we use a penalty regularization (Simo and Laursen, 1992; Yastrebov and Breitkopf, 2013; Garipov et al., 2016; Gallyamov et al., 2018) which leads to the return-mapping algorithm of

$$f_N'^{n+1} - \varepsilon_N \langle g_N^{n+1} \rangle = 0, \tag{24}$$

$$\widetilde{\boldsymbol{f}}_T' = \boldsymbol{f}_T'^n + \varepsilon_T (\boldsymbol{g}_T^{n+1} - \boldsymbol{g}_T^n), \quad \widetilde{\Phi} = \left| \widetilde{\boldsymbol{f}}_T' \right| - \mu^{n+1} f_N'^{n+1}, \tag{25}$$

$$\boldsymbol{f}_T'^{n+1} - \widetilde{\boldsymbol{f}}_T' + \langle \widetilde{\Phi} \rangle \frac{\widetilde{\boldsymbol{f}}_T'}{\left| \widetilde{\boldsymbol{f}}_T' \right|} = \mathbf{0}, \tag{26}$$

where $\widetilde{\boldsymbol{f}}_T'$ denotes a trial traction, which represents the penalized effective tangential traction (Simo and Laursen, 1992). Penalty parameters $\varepsilon_N, \varepsilon_T \gg 1$ are calculated as $\varepsilon_N = f_{scale} E \delta / V, \varepsilon_T = f_{scale} G \delta / V$ where f_{scale} is an empirical scaling factor, δ denotes the area of contact interface, V stands for mean volume of two neighbouring matrix cells, while $E and G$ denote the mean Young's and shear moduli of two neighbouring matrix cells (Cardiff et al., 2017). Moreover, the Coulomb friction function Φ used as a slipping criterion is evaluated at the trial state $\widetilde{\Phi} = \Phi(\widetilde{\boldsymbol{f}}')$ that accounts for the change of slip $\boldsymbol{g}_T$ over the time step. Macaulay brackets are used to indicate that $\langle a \rangle$ is equal to a if $a \geq 0$ and otherwise equal to zero. Thus, in the slip state $\widetilde{\Phi} = 0$ Eq. (26) requires contact to remain at the slipping surface defined by $\Phi = 0$ where the direction of forces is defined by the trial traction. Contact reaches the stick state once the slip increment in Eq. (25) becomes negligible compared to the previous traction ($\dot{\boldsymbol{g}}_T = \mathbf{0}$). In this case, Eq. (26) claims the traction to be equal to the trial one. In our experience, the return-mapping algorithm described in Eqs. (25)-(26) does not exhibit significant convergence problems, except for cases with severe inf-sup instability (pressure oscillations) and when the slip direction reverses. We may also expect convergence issues in the presence of intersecting faults or in the case of a hydraulically active fault when its volume and transmissibilities depend on the aperture g_N.

Although Eqs. (24)-(26) can be treated as boundary conditions with no extra degrees of freedom (Terekhov, 2020b), it might be convenient to treat the gap vector $\mathbf{g}$ as an unknown assigned to particular fault cells, especially in induced seismicity applications. Moreover, it allows the block structure of the Jacobian to be maintained.

The fluid mass balance in fault cells can be written as

$$V_i\left(\rho_i^{n+1}-\rho_i^n+\Delta t\, r_i^{n+1}\right)+\sum_{j\in\partial V_i}\delta_{ij}\left(\rho_i^{n+1}\tilde{q}_{f\,ij}^{\,n+1}-\rho_i^n\tilde{q}_{f\,ij}^{\,n}+\Delta t\left(\frac{\rho q_f}{\mu}\right)_{ij}^{n+1}\right)=0, \tag{27}$$

where $(\rho/\mu)_{ij}$ is taken from the upwind direction, fluxes of displacements $\tilde{q}_{ij}^n, \tilde{q}_{ij}^{n+1}$ are evaluated only between fault and matrix cells, and where the approximations of $\mathbf{f}, q$, and $\tilde{q}$ are discussed in the following sections. It is worth to point out that we expect discontinuous displacements over the fault interface whereas pressure remains continuous there according to the assumptions of the DFM approach.

The influence of mechanical stresses on the conductivity of hydraulically active faults can be of high interest in the modeling of hydraulic fracturing. Although we do not consider fault opening in this paper, this effect was addressed by other researchers using FEM with penalty regularization (Garipov et al., 2016), the Nitsche method (Garipov and Hui, 2019) or Lagrange multipliers (Franceschini et al., 2022); and in the FVM framework with using Lagrange multipliers (Berge et al., 2020). The latter development within FVM also demonstrates the applicability of our developed method to model hydraulically active faults.

Multi-point approximations

In order to complete the set of discrete equations presented in the previous section, the approximation of momentum and fluid mass at the interfaces of the computational grid must be provided. The approximation of $\tilde{q}_f$ is also required as far as Gauss' formula is used to represent terms in Eq. (23).

The approximation may be performed in a number of ways, and different interpolation strategies can be employed. As usual, for many FV schemes, the approximation is derived from the requirements of continuity of unknowns and fluxes at some point on the interface between two cells. The first requirement reflects the continuity of solutions of the balance Eqs. (1), (2). The second one imposes the conservation of momentum and fluid mass at the local scale.

In this paper, we improve the coupled multi-point stress and multi-point flux approximations at faults presented in Novikov et al. (2022). The lower-dimensional treatment of discontinuity in mechanics requires the construction of connections different from flow problems where the fault is considered according to the equidimensional DFM approach (Karimi-Fard et al., 2004). As a result, we impose the continuity between matrix-matrix cells in mechanics and between matrix-fault cells in a flow problem. In this section, we provide the derivation of these approximations at faults and the corresponding equations for gradient reconstruction. The approximations at continuous interfaces and at boundaries can be found in Terekhov (2020a).

Approximation at discontinuity. Although faults are usually represented as 2D surfaces in computational grids, DFM assigns some aperture so that they have a volume greater than zero in the discrete fluid mass balance (Karimi-Fard et al., 2004). In contrast to DFM, in mechanics we treat faults as lower-dimensional objects. It allows displacements to be discontinuous at faults while pressure remains continuous according to the assumptions of the DFM. We introduce an additional degree of freedom (d.o.f.) per fault interface, namely a gap vector $\boldsymbol{g}=\boldsymbol{u}_2^+-\boldsymbol{u}_1^-$, which is equal to the jump of displacements over the interface. Using this definition, we can impose the continuity of unknowns and fluxes

as

$$\boldsymbol{u}_1 \pm \boldsymbol{g}_3 + \left[\boldsymbol{I} \otimes (\boldsymbol{x}_3 - \boldsymbol{x}_1)^T\right](\nabla \otimes \boldsymbol{u}_1) = \boldsymbol{u}_2 + \left[\boldsymbol{I} \otimes (\boldsymbol{x}_3 - \boldsymbol{x}_2)^T\right](\nabla \otimes \boldsymbol{u}_2), \tag{28}$$

$$p_1 + (\boldsymbol{x}_\delta - \boldsymbol{x}_1) \cdot \nabla p_1 = p_3 + (\boldsymbol{x}_\delta - \boldsymbol{x}_3) \cdot \nabla p_3, \tag{29}$$

$$-\left[\boldsymbol{I} \otimes \boldsymbol{n}^T\right] \boldsymbol{Q}_1 (\nabla \otimes \boldsymbol{u}_1) = -\left[\boldsymbol{I} \otimes \boldsymbol{n}^T\right] \boldsymbol{Q}_2 (\nabla \otimes \boldsymbol{u}_2), \tag{30}$$

$$-(\nabla p_1 - \rho_f g \nabla z) \cdot \boldsymbol{K}_1 \boldsymbol{n} = -(\nabla p_3 - \rho_f g \nabla z) \cdot \boldsymbol{K}_3 \boldsymbol{n}, \tag{31}$$

where $\boldsymbol{u}_1, p_1$ and $\boldsymbol{u}_2, p_2$ denote vectors of displacements and pressure defined at the centers $\boldsymbol{x}_1$ and $\boldsymbol{x}_2$ of matrix cells 1 and 2 respectively, $\boldsymbol{g}_3$ denotes the gap vector defined at fault cell 3, and $\boldsymbol{x}_\delta$ denotes the center of the interface δ. The Kronecker product $\otimes$ works that $\boldsymbol{I} \otimes (\boldsymbol{x}_\delta - \boldsymbol{x}_i)^T, i = 1,2$ represent 3×9 matrices constructed as

$$\boldsymbol{I} \otimes (\boldsymbol{x}_\delta - \boldsymbol{x}_i)^T = \begin{pmatrix} (\boldsymbol{x}_\delta - \boldsymbol{x}_i)^T & & \\ & (\boldsymbol{x}_\delta - \boldsymbol{x}_i)^T & \\ & & (\boldsymbol{x}_\delta - \boldsymbol{x}_i)^T \end{pmatrix}, \quad i = 1,2,$$

$\nabla \otimes \boldsymbol{u}_i$ is 9×1 vector, constructed as

$$\nabla \otimes \boldsymbol{u}_i = \begin{pmatrix} \nabla u_x \\ \nabla u_y \\ \nabla u_z \end{pmatrix}_i, \quad i = 1,2, \tag{32}$$

$\boldsymbol{Q}_i = \boldsymbol{Y}\boldsymbol{C}_i\boldsymbol{Y}^T$ are 9×9 matrices, $\boldsymbol{C}_i, i = 1,2$ are 6×6 symmetric stiffness matrices defined in cell i and written in Voigt notation and

$$\boldsymbol{Y}^T = \begin{bmatrix} 1&0&0&0&0&0&0&0&0 \\ 0&0&0&0&1&0&0&0&0 \\ 0&0&0&0&0&0&0&0&1 \\ 0&0&0&0&0&1&0&1&0 \\ 0&0&1&0&0&0&1&0&0 \\ 0&1&0&1&0&0&0&0&0 \end{bmatrix}.$$

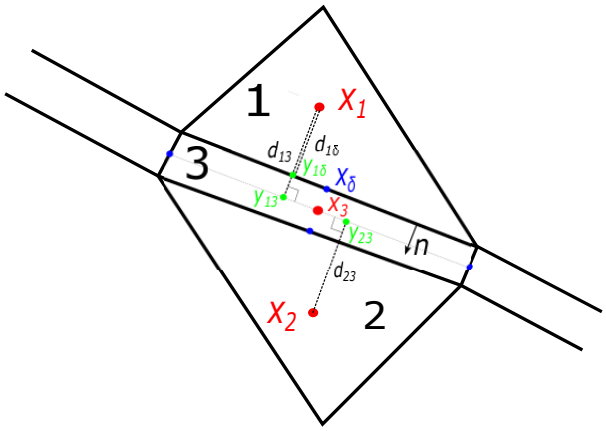

Figure 1: Geometry of a fault cell. The continuity of displacements and traction vector is imposed at the center of fault cell $\boldsymbol{x}_3$ whereas the continuity of pressure and fluid flux is imposed at the center of the interface between matrix cell 1 and fault cell 3.

Fig. 1 shows the geometry of a fault cell. The continuity of displacements in Eq. (28) is imposed at the center of fault cell $\boldsymbol{x}_3$ and the continuity of pressure at the center of the interface between matrix and fault cells $\boldsymbol{x}_\delta$. This interface is parallel to the fault and shifted over half of its aperture (perpendicularly to thefault) towards matrix cell 1.

Below we will use the following co-normal decompositions:

$$\nabla\otimes\begin{bmatrix}\boldsymbol{u}\\ p\end{bmatrix}_i=[\boldsymbol{I}\otimes\boldsymbol{n}]\boldsymbol{\xi}_i+\boldsymbol{\xi}_{\tau i},\qquad \boldsymbol{\xi}_i=[\boldsymbol{I}\otimes\boldsymbol{n}^T]\left[\nabla\otimes\begin{bmatrix}\boldsymbol{u}\\ p\end{bmatrix}_i\right],\qquad \boldsymbol{\xi}_{\tau i}=[\boldsymbol{I}\otimes(\boldsymbol{I}-\boldsymbol{n}\boldsymbol{n}^T)]\left[\nabla\otimes\begin{bmatrix}\boldsymbol{u}\\ p\end{bmatrix}_i\right], \quad (33)$$

$$\left[\boldsymbol{I}\otimes\boldsymbol{n}^T\right]\boldsymbol{Q}_i=\boldsymbol{T}_i[\boldsymbol{I}\otimes\boldsymbol{n}^T]+\boldsymbol{\Gamma}_i,\qquad \boldsymbol{T}_i=[\boldsymbol{I}\otimes\boldsymbol{n}^T]\boldsymbol{Q}_i[\boldsymbol{I}\otimes\boldsymbol{n}],\qquad \boldsymbol{\Gamma}_i=[\boldsymbol{I}\otimes\boldsymbol{n}^T]\boldsymbol{Q}_i[\boldsymbol{I}\otimes(\boldsymbol{I}-\boldsymbol{n}\boldsymbol{n}^T)], \quad (34)$$

$$\boldsymbol{K}_i\boldsymbol{n}=\kappa_i\boldsymbol{n}+\boldsymbol{\kappa}_i,\qquad \kappa_i=\boldsymbol{n}^T\boldsymbol{K}_i\boldsymbol{n},\qquad \boldsymbol{\kappa}_i=(\boldsymbol{I}-\boldsymbol{n}\boldsymbol{n}^T)\boldsymbol{K}_i\boldsymbol{n}, \quad (35)$$

$$\begin{aligned}
&\boldsymbol{x}_3-\boldsymbol{x}_1=d_{13}\boldsymbol{n}+(\boldsymbol{x}_3-\boldsymbol{y}_{13}), && d_{13}=\boldsymbol{n}\cdot(\boldsymbol{x}_3-\boldsymbol{x}_1)>0, && \boldsymbol{y}_{13}=\boldsymbol{x}_1+d_{13}\boldsymbol{n},\\
&\boldsymbol{x}_2-\boldsymbol{x}_3=d_{23}\boldsymbol{n}+(\boldsymbol{y}_{23}-\boldsymbol{x}_3), && d_{23}=\boldsymbol{n}\cdot(\boldsymbol{x}_2-\boldsymbol{x}_3)>0, && \boldsymbol{y}_{23}=\boldsymbol{x}_2-d_{23}\boldsymbol{n},\\
&\boldsymbol{x}_\delta-\boldsymbol{x}_1=d_{1\delta}\boldsymbol{n}+(\boldsymbol{x}_\delta-\boldsymbol{y}_{1\delta}), && d_{1\delta}=\boldsymbol{n}\cdot(\boldsymbol{x}_\delta-\boldsymbol{x}_1)>0, && \boldsymbol{y}_{1\delta}=\boldsymbol{x}_1+d_{1\delta}\boldsymbol{n},\\
&\boldsymbol{x}_3-\boldsymbol{x}_\delta=d_{3\delta}\boldsymbol{n}+(\boldsymbol{x}_3-\boldsymbol{y}_{3\delta}), && d_{3\delta}=\boldsymbol{n}\cdot(\boldsymbol{x}_3-\boldsymbol{x}_\delta)>0, && \boldsymbol{y}_{3\delta}=\boldsymbol{x}_3-d_{3\delta}\boldsymbol{n},
\end{aligned}$$

where subscripts $i=1,2$ refer to the matrix cells, $i=3$ refers to fault cell, d_{ij} stands for the projection of $\boldsymbol{x}_j-\boldsymbol{x}_i$ on the direction $\boldsymbol{n}$ normal to the interface while $\boldsymbol{y}_{ij}$ denotes the projection of $\boldsymbol{x}_j-\boldsymbol{x}_i$ on the direction tangential to the interface, $\boldsymbol{T}_1$ and $\boldsymbol{T}_2$ are 3×3 matrices, $\boldsymbol{\Gamma}_1$ and $\boldsymbol{\Gamma}_2$ are 3×9 matrices, while scalars κ_1 and κ_2 and vectors $\boldsymbol{\kappa}_1$ and $\boldsymbol{\kappa}_2$ provide co-normal decompositions of $\boldsymbol{K}_1\boldsymbol{n}$ and $\boldsymbol{K}_2\boldsymbol{n}$. The 3×1 vectors $\boldsymbol{\xi}_1$, $\boldsymbol{\xi}_2$ and the 9×1 vectors $\boldsymbol{\xi}_{\tau1}$, $\boldsymbol{\xi}_{\tau2}$ represent normal and tangential projections of the gradients of unknowns respectively.

Co-normal decomposition applied to Eqs. (28)-(31) gives the following equations

$$\boldsymbol{u}_1\pm\boldsymbol{g}_3+d_{13}\boldsymbol{\xi}_1^u+\left[\boldsymbol{I}\otimes(\boldsymbol{x}_3-\boldsymbol{y}_{13})^T\right]\boldsymbol{\xi}_{\tau1}^u=\boldsymbol{u}_2-d_{23}\boldsymbol{\xi}_2^u+\left[\boldsymbol{I}\otimes(\boldsymbol{x}_3-\boldsymbol{y}_{23})^T\right]\boldsymbol{\xi}_{\tau2}^u, \quad (36)$$

$$p_1+d_{1\delta}\xi_1^p+(\boldsymbol{x}_\delta-\boldsymbol{y}_{1\delta})^T\boldsymbol{\xi}_{\tau1}^p=p_3-d_{3\delta}\xi_3^p, \quad (37)$$

$$-\boldsymbol{T}_1\boldsymbol{\xi}_1^u-\boldsymbol{\Gamma}_1\boldsymbol{\xi}_{\tau1}^u=-\boldsymbol{T}_2\boldsymbol{\xi}_2^u-\boldsymbol{\Gamma}_2\boldsymbol{\xi}_{\tau2}^u, \quad (38)$$

$$-\kappa_1\xi_1^p-\boldsymbol{\kappa}_1^T\boldsymbol{\xi}_{\tau1}^p+\zeta_1=-\kappa_3\xi_3^p-\boldsymbol{\kappa}_3^T\boldsymbol{\xi}_{\tau3}^p+\zeta_3, \quad (39)$$

where $\boldsymbol{\xi}_i^u$, $\boldsymbol{\xi}_i^p$ are normal projections of displacement and pressure gradients in the vector $\boldsymbol{\xi}_i=[\boldsymbol{\xi}_i^{uT}\ \xi_i^p]^T$, $\boldsymbol{\xi}_{\tau i}^u$, $\boldsymbol{\xi}_{\tau i}^p$, $i=1,2,3$ are tangential projections of displacement and pressure gradients in the vector $\boldsymbol{\xi}_{\tau i}=[\boldsymbol{\xi}_{\tau i}^{uT}\ \boldsymbol{\xi}_{\tau i}^{pT}]^T$, $i=1,2,3$, $\zeta_i=\rho_f g\nabla z\cdot\boldsymbol{K}_i\boldsymbol{n}$, $i=1,3$. Note, that in Eqs. (38), (39) we omit Biot terms for both momentum and fluid mass fluxes.

Deriving $\boldsymbol{\xi}_2^u,\xi_3^p$ from Eqs. (36), (37) and substituting the result into Eqs. (38), (38) we obtain the following expressions for $\boldsymbol{\xi}_1^u,\xi_1^p$

$$(d_{23}\boldsymbol{T}_1+d_{13}\boldsymbol{T}_2)\,\boldsymbol{\xi}_1^u=\boldsymbol{T}_2\left(\boldsymbol{u}_2-\boldsymbol{u}_1\mp\boldsymbol{g}_3+\boldsymbol{I}\otimes(\boldsymbol{x}_3-\boldsymbol{y}_{23})^T\boldsymbol{\xi}_{\tau2}^u-\boldsymbol{I}\otimes(\boldsymbol{x}_3-\boldsymbol{y}_{13})^T\boldsymbol{\xi}_{\tau1}^u\right)+d_{23}\left(\boldsymbol{\Gamma}_2\boldsymbol{\xi}_{\tau2}^u-\boldsymbol{\Gamma}_1\boldsymbol{\xi}_{\tau1}^u\right), \quad (40)$$

$$(d_{3\delta}\kappa_1+d_{1\delta}\kappa_3)\,\xi_1^p=\kappa_2\,(p_3-p_1)+d_{3\delta}\left(\kappa_2(\boldsymbol{y}_{1\delta}-\boldsymbol{x}_\delta)^T+d_{3\delta}(\boldsymbol{\kappa}_3-\boldsymbol{\kappa}_1)\right)\boldsymbol{\xi}_\tau^p, \quad (41)$$

where $\boldsymbol{\xi}_{\tau1}^p=\boldsymbol{\xi}_{\tau3}^p=\boldsymbol{\xi}_\tau^p$ because pressure remains continuous over the interface.

Substituting Eqs. (40), (41) into the left-hand side of Eqs. (38), (39), one obtains the following multi-point approximation for the diffusive part of the fluxes at discontinuity:

$$\begin{aligned}
\boldsymbol{f}_\delta^{(d)}=&-\boldsymbol{T}\left(\boldsymbol{u}_2-\boldsymbol{u}_1\mp\boldsymbol{g}+\boldsymbol{I}\otimes(\boldsymbol{x}_3-\boldsymbol{y}_{23})^T\boldsymbol{\xi}_{\tau2}^u-\boldsymbol{I}\otimes(\boldsymbol{x}_3-\boldsymbol{y}_{13})^T\boldsymbol{\xi}_{\tau1}^u\right)-\\
&-d_{23}\boldsymbol{T}_1\left(d_{23}\boldsymbol{T}_1+d_{13}\boldsymbol{T}_2\right)^{-1}\boldsymbol{\Gamma}_2\boldsymbol{\xi}_{\tau2}^u-d_{13}\boldsymbol{T}_2\left(d_{23}\boldsymbol{T}_1+d_{13}\boldsymbol{T}_2\right)^{-1}\boldsymbol{\Gamma}_1\boldsymbol{\xi}_{\tau1}^u, \quad (42)
\end{aligned}$$

$$\begin{aligned}
q_{f\,\delta}^{(d)}=&-\kappa\left(p_3-p_1-(\boldsymbol{x}_\delta-\boldsymbol{y}_{1\delta})^T\boldsymbol{\xi}_\tau^p\right)-\\
&-d_{3\delta}\kappa_1\left(d_{3\delta}\kappa_1+d_{1\delta}\kappa_3\right)^{-1}\left(\boldsymbol{\kappa}_3\boldsymbol{\xi}_\tau^p-\boldsymbol{\zeta}_3\right)-d_{1\delta}\kappa_3\left(d_{3\delta}\kappa_1+d_{1\delta}\kappa_3\right)^{-1}\left(\boldsymbol{\kappa}_1\boldsymbol{\xi}_\tau^p-\boldsymbol{\zeta}_1\right), \quad (43)
\end{aligned}$$

where $\boldsymbol{T}=\boldsymbol{T}_1\left(d_{23}\boldsymbol{T}_1+d_{13}\boldsymbol{T}_2\right)^{-1}\boldsymbol{T}_2$, $\kappa=\kappa_1\left(d_{3\delta}\kappa_1+d_{1\delta}\kappa_3\right)^{-1}\kappa_3$.

The final approximation of the diffusive part of the traction vector is obtained as the arithmetic mean of the approximations defined in Eq. (42) written for both sides $\delta1$, $\delta2$ of the fault cell,

$$\boldsymbol{f}_\delta^{(d)}=\frac{\boldsymbol{f}_{\delta1}^{(d)}-\boldsymbol{f}_{\delta2}^{(d)}}{2}, \quad (44)$$

where "-" takes into account the fact that the approximations $\boldsymbol{f}_{\delta 1}^{(d)}, \boldsymbol{f}_{\delta 2}^{(d)}$ are defined in Eq. (42) for opposite orientations of the normal vector.

We approximate the advective part of traction vector $\boldsymbol{f}_{\delta}^{(a)}$ and flux $\tilde{q}_f$ as

$$\boldsymbol{f}_{\delta}^{(a)} = p_3 \boldsymbol{B}_3 \boldsymbol{n}, \quad \tilde{q}_{f\delta} = (\boldsymbol{B}_1 \boldsymbol{n})^T \otimes (\boldsymbol{x}_\delta - \boldsymbol{x}_1)^T \left(\nabla \otimes \boldsymbol{u}_1 - \nabla \otimes \boldsymbol{u}_{1,0}\right), \tag{45}$$

where $(\boldsymbol{B}_i \boldsymbol{n})^T \otimes (\boldsymbol{x}_\delta - \boldsymbol{x}_i)^T$ is a 1×9 row vector and $\nabla \otimes \boldsymbol{u}_{1,0}$ denotes the gradients of displacements defined Eq. (32) and are taken from the previous time step.

We use a DFM for the flow which implies having discrete equations for fracture segments of non-zero volume. The particular scheme was shown in Eq. (27). We assume continuous pressure at the boundary between fault cells. The following two-point approximation of Darcy flow is used for these connections

$$q_{f\delta} = \frac{\kappa_1 \kappa_2}{d_1 \kappa_2 + d_2 \kappa_1}(p_1 - p_2) + \rho_{f,12} g \nabla z \cdot \boldsymbol{n}, \tag{46}$$

where $\rho_{f,12} = (d_1 \rho_{f,2} + d_2 \rho_{f,1})/(d_1 + d_2)$ is linearly interpolated between cells.

Gradient reconstruction. The approximations in Eqs. (42), (43), (45) require the gradients of the unknowns to be reconstructed. One can derive $\boldsymbol{\xi}_2^u, \xi_3^p$ from Eqs. (38), (39) and substitute them into Eqs. (36), (37) to obtain the interpolation equation as

$$\begin{aligned}\left(\boldsymbol{T}_2 \otimes (\boldsymbol{x}_2 - \boldsymbol{x}_1)^T + d_{23}\left(\boldsymbol{T}_1 - \boldsymbol{T}_2\right) \otimes \boldsymbol{n}^T + d_{23}(\boldsymbol{\Gamma}_1 - \boldsymbol{\Gamma}_2)\right)\left[\nabla \otimes \boldsymbol{u}_1\right] = \\ = \boldsymbol{T}_2 \left(\boldsymbol{u}_2 - \boldsymbol{u}_1 \mp \boldsymbol{g}_3\right) \mp \left(\boldsymbol{T}_2 \otimes (\boldsymbol{y}_{23} - \boldsymbol{x}_3)^T - d_{23}\boldsymbol{\Gamma}_2\right) \nabla \otimes \boldsymbol{g}_3,\end{aligned} \tag{47}$$

$$\left(\kappa_3 (\boldsymbol{x}_3 - \boldsymbol{x}_1) + d_{3\delta}(\boldsymbol{K}_1 - \boldsymbol{K}_3)\boldsymbol{n}\right) \cdot \nabla p_1 = \kappa_3 (p_3 - p_1) + d_{3\delta}(\zeta_1 - \zeta_3). \tag{48}$$

Eq. (48) is used as a condition for pressure gradient reconstruction not only between matrix and fault cells but also between fault cells.

Gap gradients are reconstructed by using the following relation for the connections between fault cells

$$[\boldsymbol{I} \otimes (\boldsymbol{x}_2 - \boldsymbol{x}_1)^T] \nabla \otimes \boldsymbol{g}_1 = \boldsymbol{g}_2 - \boldsymbol{g}_1. \tag{49}$$

In the connection between a fault cell and an open boundary interface we have

$$\left[\boldsymbol{I} \otimes (\boldsymbol{x}_2 - \boldsymbol{x}_1)^T\right] \nabla \otimes \boldsymbol{g}_1 = 0, \tag{50}$$

whereas for a closed boundary (fault tip) we have

$$\left[\boldsymbol{I} \otimes (\boldsymbol{x}_2 - \boldsymbol{x}_1)^T\right] \nabla \otimes \boldsymbol{g}_1 = -\boldsymbol{g}_1. \tag{51}$$

It is worth to mention that these equations does not take into account material contrasts.

The condition for a connection between a matrix cell and a boundary interface can be found in Terekhov (2020a).

It is necessary to consider at least 3 interfaces (in 3D) of the first cell to enclose the system with respect to the 12 components of $\nabla \otimes \begin{pmatrix} \boldsymbol{u} \\ p \end{pmatrix}_i$. Bringing together Eqs. (47), (48) and the corresponding conditions written for continuous interfaces and boundaries (Terekhov, 2020a) for N considered interfaces of the i-th cell, we build up the system

$$\boldsymbol{M}_i \left(\nabla \otimes \begin{pmatrix} \boldsymbol{u} \\ p \end{pmatrix}_i\right) = \boldsymbol{D}_i \boldsymbol{\psi}_i, \tag{52}$$

where $\boldsymbol{M}_i$ is a $4N \times 12$ matrix and $\boldsymbol{D}_i$ is a $4N \times 4(N+1)$ matrix of coefficients in front of the corresponding unknowns at the right-hand side of these equations, while $\boldsymbol{\psi}_i$ is a $4(N+1) \times 1$ vector of $N+1$ unknowns (or free terms in the right-hand sides of the boundary conditions). The solution of Eq. (52) can be obtained in a least-squares sense as

$$\nabla \otimes \begin{pmatrix} \boldsymbol{u} \\ p \end{pmatrix}_i = (\boldsymbol{M}_i^T \boldsymbol{M}_i)^{-1} \boldsymbol{M}_i^T \boldsymbol{D}_i \boldsymbol{\psi}_i. \tag{53}$$

For the approximation of tangential gradients $\boldsymbol{\xi}_\tau = [\boldsymbol{\xi}_\tau^{uT} \; \boldsymbol{\xi}_\tau^{pT}]^T$ in Eq. (43) the following combination of gradients is used (Terekhov, 2020a):

$$\boldsymbol{\xi}_\tau = \frac{\boldsymbol{\xi}_{\tau 1} + \boldsymbol{\xi}_{\tau 2}}{2}. \tag{54}$$

A set of cells that contribute to the approximation Eq. (54) for each interface of some cell i is illustrated in Fig. 2.

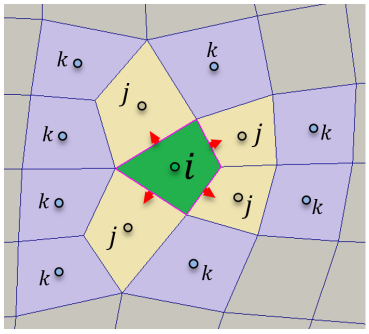

Figure 2: Cells that contribute to the approximation of fluxes over the interfaces of cell i. Index j denotes the nearest neighbours of cell i. Index k denotes farther neighbours that contribute to the gradients reconstructed in cells j.

Note that the least-squares solution in Eq. (53) allows computing the gradients of unknowns locally and independently for every cell. Note, however, that it does not guarantee the local conservation property for the scheme. It can be maintained if individual gradients for every interface that respects the corresponding flux balance are employed.

Solution strategy

The approach to discretization presented in the previous section allows the approximation of momentum and fluid mass fluxes to be calculated only once before iteration over time. Nonlinearity introduced by fluid density and viscosity can be taken into account having the equations for fluid mass flux in Eq. (10) and flux of displacements in Eq. (22) already approximated. It requires the assembly of Darcy and Hooke (diffusive) terms separate from Biot (advective) terms. Fluid gravity taken in $\boldsymbol{\zeta}_i$ should be assembled also separately in order to be multiplied by pressure-dependent fluid density.

We use Newton iterations at every time step to resolve nonlinearity exhibited by contact conditions and fluid properties. In the current study, we employ a direct solver for the linear system of equations. An advanced preconditioning strategy for the iterative linear solver applied to a similar system is described in Novikov et al. (2022).

Results

Displaced reservoir

Faulted reservoirs can experience different mechanical conditions over their geological history. Nearly always this results in an offset such that stratigraphic layers become displaced. An analytical investigation of stresses initiated around a displaced fault in a depleted reservoir is carried out in Jansen et al.

(2019); Jansen and Meulenbroek (2022). In this test case, we compare the solution we obtain numerically against the analytical one.

The square model domain shown in Fig. 3a of size $L = W = 4500\,\text{m}$ is considered with shear modulus $G = 6.5\,\text{GPa}$ and Poisson ratio $\nu = 0.15$. A fault inclined by $\theta = 70^{\text{o}}$ with respect to the horizontal axis crosses the center of the domain. The reservoir is displaced over this fault in a way that the left side lies between $a = 75\,\text{m}$ above and $b = 150\,\text{m}$ below the horizontal centerline of the domain, and vice versa for the right side. A Biot coefficient $b = 0.9$ is used inside the reservoir. The domain is subjected to gravitational forces distributed over the domain according to its density defined in Eq. (7) where $\rho_f = 1020\,\text{kg/m}^3$, $\rho_s = 2650\,\text{kg/m}^3$ and $\phi = 0.15$ is constant over the whole domain. Initial pore pressure inside the domain is also governed by a gravitational gradient $p = p_0 - \rho_f g y$ where $y = 0$ corresponds to the horizontal centerline of the domain. Biot effective stresses are used in the Coulomb slipping criterion along with a static friction law (Eq. (18)) where the friction coefficient $\mu_{st} = 0.52$.

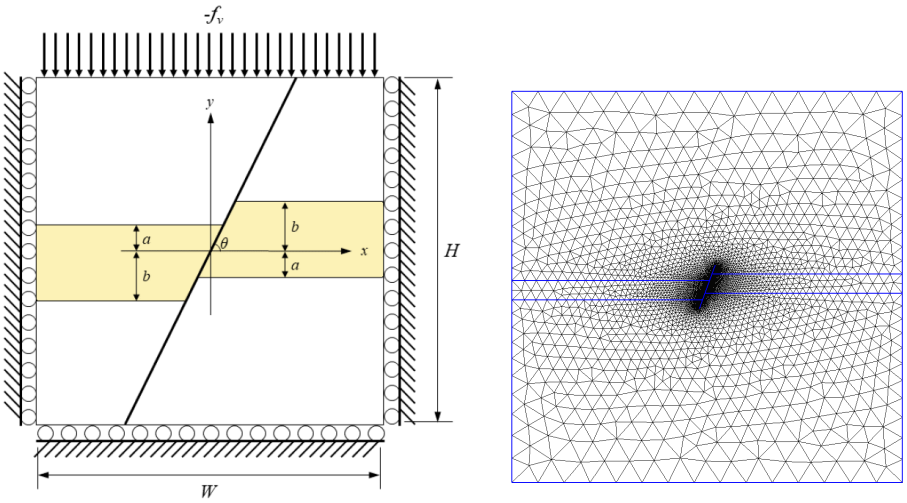

(a) (b)

Figure 3: Model geometry (a) and computational grid (b) in displaced reservoir test case.

A plane-strain 2D setup is considered. A roller boundary condition governs deformation at the bottom. A constant vertical force $f_v = \Sigma''_{yy}(H/2)$ loads the top boundary of domain, where $\Sigma''_{yy} = \rho_t g(y - D_0)$ and $D_0 = 3500\,\text{m}$. The left and right sides are subjected to compressive horizontal forces $f_h = -K_0\left(\Sigma''_{yy} + bp(y)\right) + bp(y)$, where $K_0 = 0.5$. However, this combination of boundary conditions makes the horizontal displacement u_x undefined. In order to define the problem completely, we imposed a normal Dirichlet condition at three extra boundary points and calculated the resulting displacements $u_x = u_x(y)$ over the left and right boundaries. In the current comparison, we apply these displacements as normal boundary conditions and zero force as the tangential ones. Fig. 3a shows the setup geometry and boundary conditions, while the grid used in modelling is presented in Fig. 3b.

We consider an instantaneous constant depletion Δp inside the reservoir. The displaced geometry of the reservoir produces discontinuous shear stress at the four corner points of the reservoir at the fault-reservoir intersection (Jansen et al., 2019). As a result, pressure depletion leads to the development of two slip patches around the two inner points.

Jansen and Meulenbroek (2022) provide a semi-analytical solution for the slip distribution corresponding to this problem, assuming a domain of infinite horizontal extent. In Fig. 4, the calculated post-slip Coulomb stress and the slip profiles in a domain of $4W$ width are presented along with their analytical counterparts.

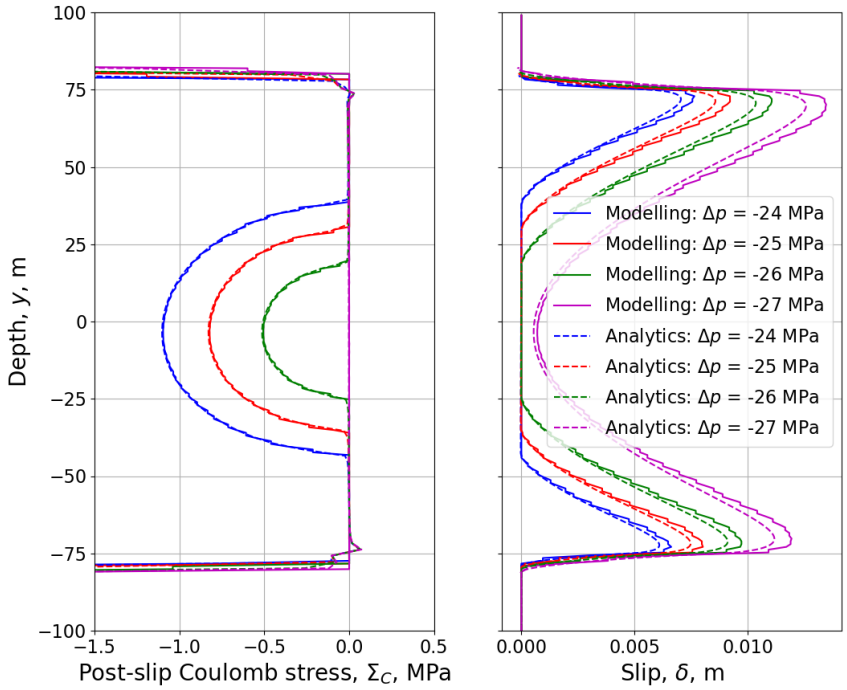

Figure 4: Post-slip Coulomb stress (left) and slip profiles (right) calculated for four values of pressure depletion $\Delta p = -24, -25, -26, -27$ MPa. Numerically calculated profiles provide a good match to their analytical counterparts.

Core injection experiment

The developed framework has also been applied to model fluid-induced fault slip behavior observed in a core injection experiment (Wang et al., 2020a). The authors performed two fluid-induced slip experiments (SC1, SC2) conducted on permeable Bentheim sandstone samples crosscut by a fault. Fault slip was triggered by fluid injection into the core at different rates. Wang et al. (2020a) measured slip, slip velocity, normal and shear stresses, and computed the apparent friction coefficient as a function of time.

In order to approximately simulate the experiment, the following setup is considered. A rectangular 2D domain (Fig. 5) of 50×100 mm size is loaded from the left and the right with a confining normal stress $|\mathbf{f}| = 350$ bar, and from the top by a constant displacement $u_y = -0.385$ mm in SC1 and $u_y = -0.36$ mm in SC2. A roller condition is specified for the tangential degree of freedom at the top boundary whereas the displacements at the bottom boundary are fixed. Following the post-processing of experimental results (Wang et al., 2020a) we apply plane strain conditions to the third dimension. The domain has constant Young's modulus 26 GPa, Poisson's ratio $\nu = 0.17$, an isotropic Biot tensor $\boldsymbol{B} = \mathrm{diag}(0.6, 0.6, 0.6)$, an isotropic permeability tensor $\boldsymbol{K} = \mathrm{diag}(1,1,1)$ Darcy, porosity $\phi_0 = 0.23$ and constant compressibility $1.45 \cdot 10^{-10}\,\mathrm{Pa}^{-1}$. The fault has the same permeability as the matrix.

The normal displacements applied from the top are chosen to match the initial vertical stress (σ_1 in Wang et al. (2020a)) observed in the experiment. Using a Neumann condition for the top boundary directly is not possible because once the fault starts sliding, the problem becomes purely Neumann so that the displacements in the top piece become only defined up to an arbitrary constant.

Water of constant viscosity $\mu = 10^{-3}\mathrm{Pa}\cdot\mathrm{s}$ and compressibility $10^{-9}\,\mathrm{Pa}^{-1}$ is injected into the domain through the bottom boundary at a specified pressure $p = p(t)$ whereas the other boundaries are im-

permeable. The evolution of injection pressure and friction coefficient are taken precisely from the experimental data and are shown in Fig. 6. The injection pressure is increased step-wise in SC1 while in SC2 it is increased gradually while keeping the pressure constant during short periods of time.

Fig. 6 depicts the dynamics of experimental slip, slip velocity, normal and shear stresses compared to their counterparts calculated numerically with a time step $\Delta t = 2\,\mathrm{s}$. Although we used a 2D approximation of a 3D setup, there is a good match in terms of slip, both stresses, and slip velocity in both tests.

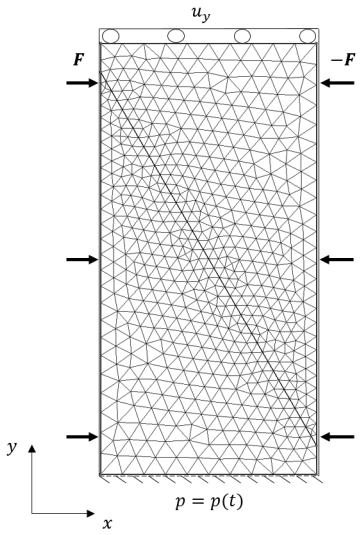

Figure 5: Model setup.

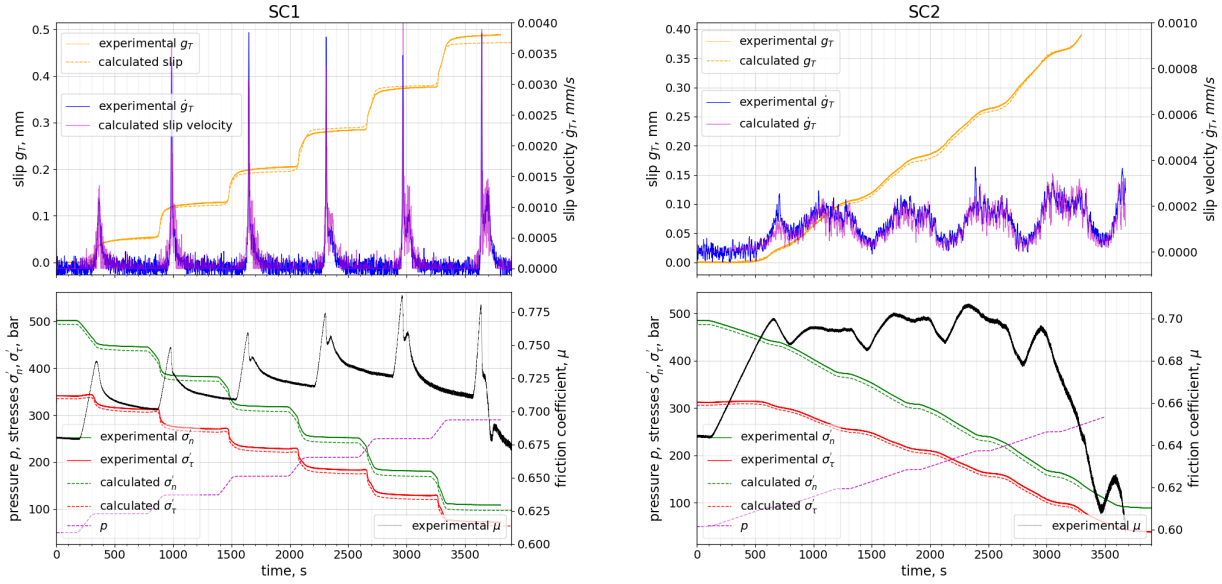

Figure 6: Numerical simulation of core injection experiments from Wang et al. (2020a). Two injection scenarios were considered: step-wise increase (SC1) and gradual increase (SC2) of injection pressure from 50 to 350 bar. The time-dependent friction coefficient was taken from the experiment.

In the first example, we use the friction coefficient calculated from the experimental data. In the second one,we employ the steady-state friction law defined in Eq. (19). A comparison of the friction coefficients obtained in modelling and measured in the experiment is shown in Fig. 7. The calculated friction coefficient manages to qualitatively represent the behavior observed in the experiment except during the final stage of SC2 where strong slip-weakening is exhibited.

The use of rate-dependent friction laws is complicated by the fact that friction goes to infinity in Eq. (19) when the slip velocity is equal to zero. One of the options is to use a regularized rate-and-state friction law (Lapusta et al., 2000). In this modeling we impose a cut-off on the magnitude of the slip velocity $v_{co} = 0.01v^*$. Below this cut-off $|\dot{\boldsymbol{g}}_T| < v_{co}$ we assume the friction coefficient to remain equal to the reference value $\mu = \mu^*$. Another complication is that under the quasi-static assumption we may not observe the slip velocity to remain continuous over time. As a result, rate-dependent friction may exhibit noisy behavior. The results shown in Fig. 7 are calculated with a large time step $\Delta t = 20\,\text{s}$. The use of smaller time steps leads to more frequent oscillations in slip velocity and in friction.

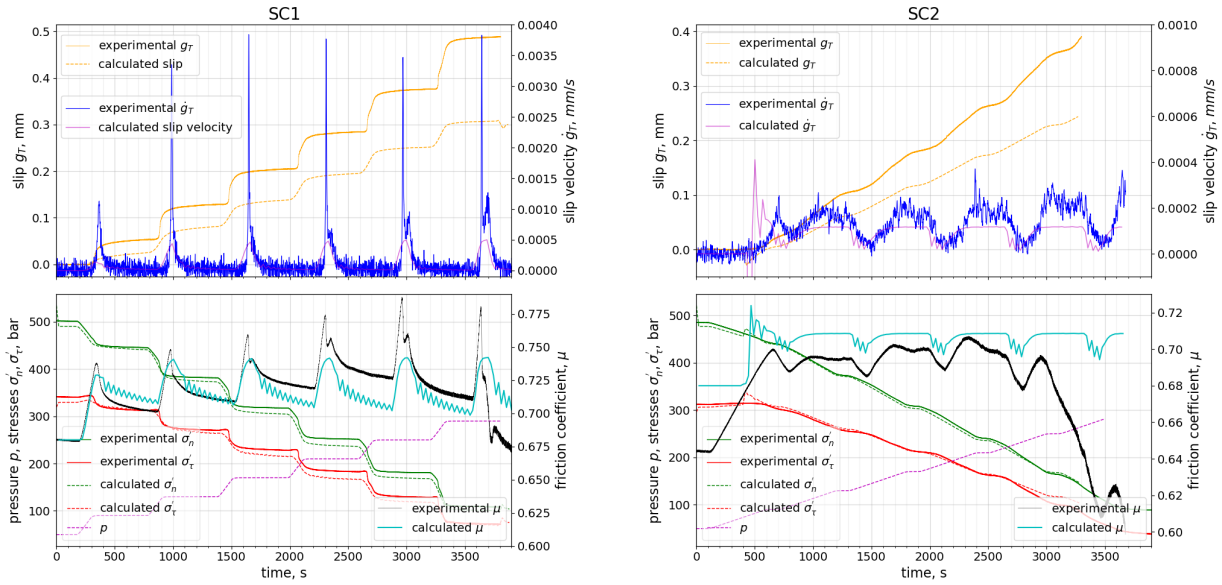

Figure 7: Numerical simulation of core injection experiments from Wang et al. (2020a). Two injection scenarios were considered: step-wise increase (SC1) and gradual increase (SC2) of injection pressure from 50 to 350 bar. Steady-state friction law defined in Eq. (19) is used, where $\mu^* = 0.68$, $a - b = 0.01$, $v^* = 1\,\text{nm/s}$ in experiment SC1, and $\mu^* = 0.68$, $a - b = 0.006$, $v^* = 1\,\text{nm/s}$ in experiment SC2.

Conclusion

We have developed a fully implicit collocated Finite Volume scheme for a faulted porous media. The improved formulation of multi-point approximations of momentum and fluid mass fluxes at faults leads to a more accurate scheme compared to our earlier implementation (Novikov et al., 2022). A collocated grid allows assigning unknowns and material properties in the same regions such that the block structure of the Jacobian is maintained. A fully coupled approximation provides a robust and unified framework to approach hydromechanical problems. Based on the literature (Terekhov, 2020a; Terekhov and Vassilevski, 2022), we expect that our method can be extended to more complex grid geometries.

The method can cope with discontinuities in displacements, as occur in faults, on the level of discretization. The multi-point approach allows to perform discretization only once in the pre-processing stage. These discrete terms remain valid for different contact states. We introduced gap degrees of freedom over the fault, which significantly simplified the formulation of contact conditions and nonlinear friction laws. We validated the method against analytical solutions and experimental results in several test cases. The developed framework demonstrates its applicability to resolve fault reactivation. The presented methodology allowed us to successfully consider nonlinear friction laws in coupled hydro-geomechanics simulation.

Acknowledgments

This publication is part of the project “Science4Steer: a scientific basis for production and reinjection strategies to minimize induced seismicity in Dutch gas fields” (with project number DEEP.NL.2018.046)

of the research program “DeepNL” which is financed by the Dutch Research Council (NWO).

Nomenclature

Physical variables

a, b – parameters of rate-and-state friction law,
$\alpha_n, \alpha_t, \alpha_p, \beta_n, \beta_t, \beta_p, \gamma_n, \boldsymbol{\gamma}_t, \gamma_p$ – coefficients that determine boundary conditions,
$\boldsymbol{B}$ – rank-two Biot tensor,
$\mathbb{C}$ – rank-four drained stiffness tensor of skeleton,
$\boldsymbol{C}$ – 6×6 symmetric matrix of stiffness coefficients,
$\boldsymbol{E}$ – rank-two strain tensor,
E – Young’s modulus,
$\boldsymbol{f}$ – traction vector,
$f_N, \boldsymbol{f}_T$ – normal and tangential projections of traction vector,
$\boldsymbol{f}'$ – effective Terzaghi traction vector,
$f'_N, \boldsymbol{f}'_T$ – normal and tangential projections of effective Terzaghi traction vector,
G – shear modulus,
$\boldsymbol{g}$ – 3×1 vector of gap in displacements,
$\boldsymbol{g}_N, \boldsymbol{g}_T$ – normal and tangential projections of gap vector,
$\dot{\boldsymbol{g}}_T$ – slip velocity vector,
g – gravity constant,
μ – friction coefficient,
μ_s – static friction coefficient,
μ^* – reference friction coefficient,
$\boldsymbol{I}$ – identity matrix of appropriate dimension,
$\boldsymbol{K}$ – rank-two tensor of permeability,
K_r – bulk modulus of the solid phase,
K_d – drained bulk modulus,
k_x, k_y, k_z – diagonal components of permeability tensor,
M – Biot’s modulus,
μ_f – fluid viscosity,
μ – friction coefficient,
$\boldsymbol{n}$ – unit normal vector,
ν – Poisson’s ratio,
p – pore pressure,
q_f – fluid flux,
r – source (sink) of fluid mass,
ρ_f – fluid density,
ρ_s – rock density,
ρ_t – total density of the medium,
$\boldsymbol{\Sigma}$ – rank-two total stress tensor,
$\boldsymbol{\Sigma}'$ – rank-two effective Terzaghi stress tensor,
$\boldsymbol{\Sigma}''$ – rank-two effective Biot stress tensor,
$\boldsymbol{\Sigma}$ – total stress tensor in Voigt notation,
$\boldsymbol{\Sigma}'$ – effective Terzaghi stress tensor in Voigt notation,
$\boldsymbol{\Sigma}''$ – effective Biot stress tensor in Voigt notation,
t – time,
$\boldsymbol{u} = [u_x u_y u_z]^T$ – vector of displacements,
$\boldsymbol{u}^-, \boldsymbol{u}^-$ – displacements at the particular side of the fault
$(\nabla \boldsymbol{u})^T$ – Jacobian matrix of $\boldsymbol{u}$
$\boldsymbol{v}$ – Darcy’s velocity of fluid,

v^* – reference slip velocity,
$\Phi = |\boldsymbol{f}'_T| - \mu f'_N$ – Coulomb function,
ϕ – porosity,
$\tilde{\phi} = \phi_0 + (p - p_0)(\psi - \phi_0)/K_r$,
$\psi = (\boldsymbol{B} : \boldsymbol{I}) / 3$ – one-third of the trace of tensor $\boldsymbol{B}$,
z – depth,
∇z – direction vector $[0\ 0\ 1]^T$.

Numerical variables

$\mathfrak{a}_i$ – accumulation vector in discrete equations for cell i,
$\boldsymbol{\kappa}_i$ – tangential projections of co-normal permeability vector,
$\boldsymbol{\Gamma}_i$ – 3×9 matrices,
Δt – time step size,
δ_j – area of interface j,
$\varepsilon_N, \varepsilon_T$ – penalty parameters,
$\mathfrak{f}_{ij}$ – flux vector in discrete equations for cell i,
$\widetilde{\boldsymbol{f}}'_T$ – penalized Terzaghi effective tangential traction,
ζ_i – gravity contribution to single-side approximations of fluid mass fluxes,
κ_i – tangential projection of co-normal permeability vector,
$\boldsymbol{\xi}_i, \boldsymbol{\xi}_{\tau i}$ – 4×1 and 12×1 vectors of normal and tangential projections of the gradients of unknowns in cell i,
$\boldsymbol{\xi}^u_i, \xi^p_i; \boldsymbol{\xi}^u_{\tau i}, \boldsymbol{\xi}^p_{\tau i}$ – normal and tangential projections of the displacement (u) and pressure (p) gradients in cell i,
$\boldsymbol{Q}_i$ – 9×9 matrix,
r_i – distance between the center of cell i and interface,
V_i – volume of cell i,
$\boldsymbol{x}_i$ – center of cell i,
$\boldsymbol{x}_\delta$ – center of the interface,
$\boldsymbol{Y}$ – 9×6 matrix,
$\boldsymbol{y}_i$ – projection of the center of cell i center on interface.

References

Berge, R., Berre, I., Keilegavlen, E., Nordbotten, J. and Wohlmuth, B. [2020] Finite volume discretization for poroelastic media with fractures modeled by contact mechanics. *International Journal for Numerical Methods in Engineering*, **121**(4), 644–663.

Berre, I., Boon, W., Flemisch, B., Fumagalli, A., Gläser, D., Keilegavlen, E., Scotti, A., Stefansson, I., Tatomir, A., Brenner, K., Burbulla, S., Devloo, P., Duran, O., Favino, M., Hennicker, J., Lee, I.H., Lipnikov, K., Masson, R., Mosthaf, K., Nestola, M., Ni, C.F., Nikitin, K., Schädle, P., Svyatskiy, D., Yanbarisov, R. and Zulian, P. [2021] Verification benchmarks for single-phase flow in three-dimensional fractured porous media. *Advances in Water Resources*, **147**.

Buijze, L., Guo, Y., Niemeijer, A., Ma, S. and Spiers, C. [2020a] Nucleation of Stick-Slip Instability Within a Large-Scale Experimental Fault: Effects of Stress Heterogeneities Due to Loading and Gouge Layer Compaction. *Journal of Geophysical Research: Solid Earth*, **125**(8).

Buijze, L., Van Bijsterveldt, L., Cremer, H., Paap, B., Veldkamp, H., Wassing, B.B., Van Wees, J.D., Van Yperen, G.C. and Ter Heege, J.H. [2020b] Review of induced seismicity in geothermal systems worldwide and implications for geothermal systems in the Netherlands. *Geologie en Mijnbouw/Netherlands Journal of Geosciences*. Cited by: 16; All Open Access, Gold Open Access, Green Open Access.

Cardiff, P., Tukovic, Z., Jaeger, P.D., Clancy, M. and Ivankovic, A. [2017] A Lagrangian cell-centred

finite volume method for metal forming simulation. *International Journal for Numerical Methods in Engineering*, **109**(13), 1777–1803.

Chen, J. and Spiers, C.J. [2016] Rate and state frictional and healing behavior of carbonate fault gouge explained using microphysical model. *Journal of Geophysical Research: Solid Earth*, **121**(12), 8642 – 8665. Cited by: 62.

Coussy, O. [2003] *Thermoporoelasticity*, chap. 4. John Wiley & Sons, Ltd, 71–112.

Deb, R. and Jenny, P. [2017a] Finite volume–based modeling of flow-induced shear failure along fracture manifolds. *International Journal for Numerical and Analytical Methods in Geomechanics*, **41**(18), 1922–1942.

Deb, R. and Jenny, P. [2017b] Modeling of shear failure in fractured reservoirs with a porous matrix. *Computational Geosciences*, **21**(5-6), 1119–1134.

Dieterich, J.H. [1979] Modeling of rock friction 1. Experimental results and constitutive equations. *Journal of Geophysical Research: Solid Earth*, **84**(B5), 2161 – 2168.

Franceschini, A., Gazzola, L. and Ferronato, M. [2022] A scalable preconditioning framework for stabilized contact mechanics with hydraulically active fractures. *Journal of Computational Physics*, **463**.

Gallyamov, E., Garipov, T., Voskov, D. and Van den Hoek, P. [2018] Discrete fracture model for simulating waterflooding processes under fracturing conditions. *International Journal for Numerical and Analytical Methods in Geomechanics*, **42**(13), 1445–1470.

Garipov, T. and Hui, M. [2019] Discrete Fracture Modeling approach for simulating coupled thermo-hydro-mechanical effects in fractured reservoirs. *International Journal of Rock Mechanics and Mining Sciences*, **122**.

Garipov, T., Karimi-Fard, M. and Tchelepi, H. [2016] Discrete fracture model for coupled flow and geomechanics. *Computational Geosciences*, **20**(1), 149–160.

Guglielmi, Y., Cappa, F., Avouac, J.P., Henry, P. and Elsworth, D. [2015] Seismicity triggered by fluid injection-induced aseismic slip. *Science*, **348**(6240), 1224–1226.

Jansen, J., Singhal, P. and Vossepoel, F. [2019] Insights From Closed-Form Expressions for Injection- and Production-Induced Stresses in Displaced Faults. *Journal of Geophysical Research: Solid Earth*, **124**(7), 7193–7212.

Jansen, J.D. and Meulenbroek, B. [2022] Induced aseismic slip and the onset of seismicity in displaced faults. *Netherlands Journal of Geosciences*, **101**, e13.

Jha, B. and Juanes, R. [2014] Coupled multiphase flow and poromechanics: A computational model of pore pressure effects on fault slip and earthquake triggering. *Water Resources Research*, **50**(5), 3776–3808.

Kala, K. and Voskov, D. [2020] Element balance formulation in reactive compositional flow and transport with parameterization technique. *Computational Geosciences*, **24**(2), 609–624.

Karimi-Fard, M., Durlofsky, L. and Aziz, K. [2004] An efficient discrete-fracture model applicable for general-purpose reservoir simulators. *SPE Journal*, **9**(2), 227–236.

Khait, M. and Voskov, D. [2018a] Adaptive parameterization for solving of thermal/compositional nonlinear flow and transport with buoyancy. *SPE Journal*, **23**(2), 522–534.

Khait, M. and Voskov, D. [2018b] Operator-based linearization for efficient modeling of geothermal processes. *Geothermics*, **74**, 7–18.

Lapusta, N., Rice, J.R., Ben-Zion, Y. and Zheng, G. [2000] Elastodynamic analysis for slow tectonic loading with spontaneous rupture episodes on faults with rate- and state-dependent friction. *Journal of Geophysical Research: Solid Earth*, **105**(B10), 23765 – 23789. Cited by: 378; All Open Access, Bronze Open Access, Green Open Access.

Li, L. and Lee, S. [2008] Efficient field-scale simulation of black oil in a naturally fractured reservoir through discrete fracture networks and homogenized media. *SPE Reservoir Evaluation and Engineering*, **11**(4), 750–758.

Lyu, X., Khait, M. and Voskov, D. [2021a] Operator-based linearization approach for modeling of multiphase flow with buoyancy and capillarity. *SPE Journal*, **26**(4), 1858–1878.

Lyu, X., Voskov, D. and Rossen, W. [2021b] Numerical investigations of foam-assisted CO2 storage in saline aquifers. *International Journal of Greenhouse Gas Control*, **108**.

Nordbotten, J. [2014] Cell-centered finite volume discretizations for deformable porous media. *International Journal for Numerical Methods in Engineering*, **100**(6), 399–418.

Novikov, A., Voskov, D., Khait, M., H., H. and Jansen, J. [2022] A Scalable Collocated Finite Volume Scheme for Simulation of Induced Seismicity. *Submitted for publication in Journal of Computational*

Physics.

Ruina, A. [1983] Slip instability and state variable friction laws. *Journal of Geophysical Research*, **88**(B12), 10359 – 10370.

Segall, P., Grasso, J.R. and Mossop, A. [1994] Poroelastic stressing and induced seismicity near the Lacq gas field, southwestern France. *Journal of Geophysical Research*, **99**(B8), 15,423–15,438.

Shapiro, S., Krüger, O., Dinske, C. and Langenbruch, C. [2011] Magnitudes of induced earthquakes and geometric scales of fluid-stimulated rock volumes. *Geophysics*, **76**(6), WC55–WC63.

Shokrollahzadeh Behbahani, S., Hajibeygi, H., Voskov, D. and Jansen, J.D. [2022] Smoothed embedded finite-volume method (sEFVM) for modeling contact mechanics in deformable faulted and fractured porous media. *Journal of Computational Physics*, **459**.

Simo, J. and Laursen, T. [1992] An augmented lagrangian treatment of contact problems involving friction. *Computers and Structures*, **42**(1), 97–116.

Sokolova, I., Bastisya, M. and Hajibeygi, H. [2019] Multiscale finite volume method for finite-volume-based simulation of poroelasticity. *Journal of Computational Physics*, **379**, 309–324.

Tene, M., Bosma, S., Al Kobaisi, M. and Hajibeygi, H. [2017] Projection-based Embedded Discrete Fracture Model (pEDFM). *Advances in Water Resources*, **105**, 205–216.

Terekhov, K. [2020a] Cell-centered finite-volume method for heterogeneous anisotropic poromechanics problem. *Journal of Computational and Applied Mathematics*, **365**.

Terekhov, K. [2020b] Multi-physics flux coupling for hydraulic fracturing modelling within INMOST platform. *Russian Journal of Numerical Analysis and Mathematical Modelling*, **35**(4), 223–237.

Terekhov, K. and Tchelepi, H. [2020] Cell-centered finite-volume method for elastic deformation of heterogeneous media with full-tensor properties. *Journal of Computational and Applied Mathematics*, **364**.

Terekhov, K.M. and Vassilevski, Y.V. [2022] Finite volume method for coupled subsurface flow problems, II: Poroelasticity. *Journal of Computational Physics*, **462**.

Ucar, E., Keilegavlen, E., Berre, I. and Nordbotten, J.M. [2018] A finite-volume discretization for deformation of fractured media. *Computational Geosciences*, **22**(4), 993 – 1007. Cited by: 19; All Open Access, Green Open Access.

Wang, L., Kwiatek, G., Rybacki, E., Bonnelye, A., Bohnhoff, M. and Dresen, G. [2020a] Laboratory Study on Fluid-Induced Fault Slip Behavior: The Role of Fluid Pressurization Rate. *Geophysical Research Letters*, **47**(6).

Wang, Y., Voskov, D., Khait, M. and Bruhn, D. [2020b] An efficient numerical simulator for geothermal simulation: A benchmark study. *Applied Energy*, **264**.

Xu, F., Hajibeygi, H. and Sluys, L. [2021] Multiscale extended finite element method for deformable fractured porous media. *Journal of Computational Physics*, **436**.

Yastrebov, V.A. and Breitkopf, P. [2013] *Numerical Methods in Contact Mechanics*.

Zhao, Y. and Borja, R. [2020] A continuum framework for coupled solid deformation–fluid flow through anisotropic elastoplastic porous media. *Computer Methods in Applied Mechanics and Engineering*, **369**.

Zoback, M. [2007] *Reservoir Geomechanics*. Cambridge University Press.